JGR Space Physics

RESEARCH ARTICLE
10.1029/2021JA029881

Phosphorus Chemistry in the Earth's Upper Atmosphere

John M. C. Plane[1], Wuhu Feng[1,2], and Kevin M. Douglas[1]

[1]School of Chemistry, University of Leeds, Leeds, UK, [2]National Centre for Atmospheric Science and School of Earth and Environment, University of Leeds, Leeds, UK

Key Points:

- A reaction network is developed in a global model for exploring the chemistry of meteor-ablated phosphorus in the Earth's upper atmosphere
- A narrow layer of OPO is predicted to occur globally around 90 km, analogous to the layers of meteor-ablated Na and Fe
- A significant flux of bio-available metal phosphites is predicted to be deposited at the Earth's surface

Supporting Information:

Supporting Information may be found in the online version of this article.

Correspondence to:

J. M. C. Plane,
j.m.c.plane@leeds.ac.uk

Citation:

Plane, J. M. C., Feng, W., & Douglas, K. M. (2021). Phosphorus chemistry in the Earth's upper atmosphere. *Journal of Geophysical Research: Space Physics*, *126*, e2021JA029881. https://doi.org/10.1029/2021JA029881

Received 12 AUG 2021
Accepted 6 SEP 2021

Abstract The ablation of phosphorus from interplanetary dust particles entering the Earth's atmosphere is a potentially significant source of this key bioelement. In this study, the atmospheric chemistry of phosphorus is explored by developing a reaction network of possible routes from PO, the major ablation product in the upper mesosphere/lower thermosphere region, to the stable reservoirs H_3PO_3 and H_3PO_4 that become incorporated into meteoric smoke particles (MSPs) as metal phosphites and phosphates, respectively. The network is constructed with reactions whose kinetics have been measured experimentally, together with reactions where theoretical rate coefficients are estimated using a combination of electronic structure theory calculations and a Rice-Ramsperger-Kassel-Markus master equation treatment. The network is then incorporated into a global chemistry-climate model, together with a phosphorus meteoric input function. The estimated global mean P deposition flux, in the form of submicron-sized MSPs, is 1×10^{-8} g m^{-2} yr^{-1}, with a maximum of $\sim 5 \times 10^{-8}$ g m^{-2} yr^{-1} over the northern Rockies, Himalayas, and southern Andes. The estimated fraction of ablated phosphorus forming bioavailable metal phosphites is 11%, which results from the very large concentrations of O and H compared to OH in the upper mesosphere. A layer of OPO is predicted to occur at 90 km with a peak of concentration of $\sim$50 cm^{-3}; this is the counterpart of the well-known layers of meteoric metals such as Na and Fe, and may be observable spectroscopically.

1. Introduction

Phosphorus is a key element in biomolecules (e.g., RNA, DNA, phospholipids, and ATP/ADP) and therefore plays important roles in replication, information transfer, and metabolism (Maciá, 2005). Although the dominant form of inorganic P at the Earth's surface is orthophosphate (PO_4^{3-}, oxidation state +5), phosphate salts have low water solubility and reactivity, which severely limits their bio-availability. Therefore, a major question concerning the development of early life on Earth was the availability of prebiotic P in its reduced forms, phosphides (P^-, oxidation state −1), phosphites (HPO_3^{2-}, oxidation state +3) or hypophosphites ($H_2PO_2^-$, oxidation state +3), which are more biologically active than the fully oxidized phosphate. Phosphorus is thought to have limited ocean primary productivity over geological timescales, and the P cycle may have constrained the slow oxygenation of the Earth's surface during the first 3.5 billion years (Lyons et al., 2014). In support of this hypothesis of P bio-limitation, Reinhard et al. (2017) have shown recently that, until around 800 million years ago, the P in shallow marine environments was significantly lower than the Redfield ratio (Redfield, 1958).

Because phosphorus is a siderophile element, the P that was present when the Earth formed should be sequestered in the molten core; hence, extraterrestrial P was probably the major source of prebiotic phosphorus at the planet's surface (Pasek, 2008). Previous studies have focused on the direct delivery of P to the surface in meteorites, where metal phosphides (in particular the mineral schreibersite, $(FeNi)_3P$) were then processed into bioavailable forms of P through aqueous-phase chemistry (Gibard et al., 2019; Pasek, 2008). A very recent study has shown that cloud-ground lightning strikes reduce phosphate in meteorites, and estimated that lightning strikes on early Earth might have formed 10–1,000 kg of phosphide and 100–10,000 kg of phosphite and hypophosphite annually (Hess et al., 2021).

In the present paper, we consider the ablation of P from interplanetary dust particles (IDPs) entering the Earth's atmosphere and its subsequent atmospheric chemistry. This potential source of reduced P does not appear to have been investigated previously. Most IDPs have a mass ranging from 10^{-3} to 100 μg (radius 2–200 μm), and a substantial fraction of the IDP mass ablates due to aerobraking at heights between 70 and 110 km (Carrillo-Sánchez, Gómez-Martín, et al., 2020). We recently performed a laboratory study

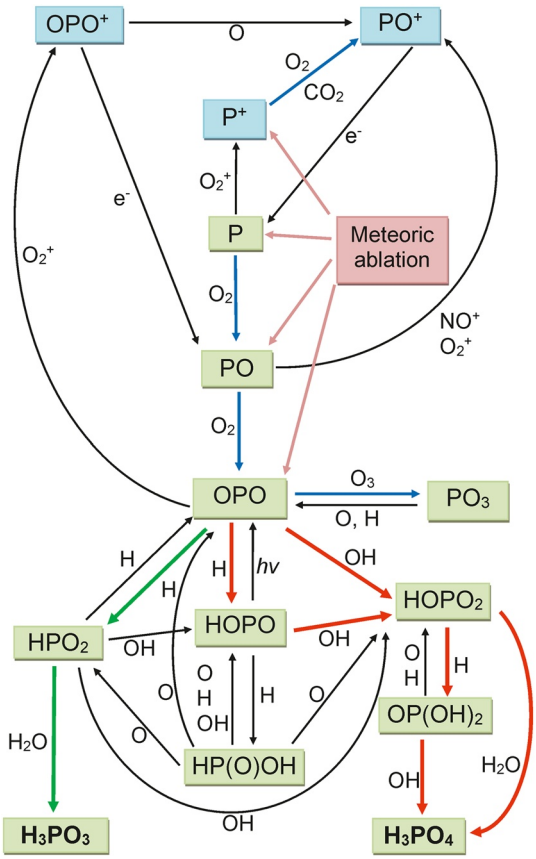

Figure 1. Schematic diagram of the neutral and ion-molecule chemistry of phosphorus in the Earth's mesosphere and lower thermosphere. Neutral and ionized P species are shown in green and blue boxes, respectively. The green arrows indicate the important pathway from OPO to H_3PO_3; the red arrows show the reactions forming H_3PO_4; the blue arrows indicate reactions that have been studied experimentally.

of phosphorus ablation from μm-size meteoritic particles, which were flash-heated to temperatures as high as 2900 K in a Meteoric Ablation Simulator (MASI), and the ablation of PO and Ca recorded simultaneously by laser-induced fluorescence (Carrillo-Sánchez, Bones, et al., 2020). In the same study, we showed using XANES spectroscopy that phosphorus in anhydrous chondritic porous IDPs mainly occurs in phosphate-like domains. A thermodynamic model of phosphorus in a silicate melt was then developed for inclusion in the Leeds Chemical Ablation Model (CABMOD) (Vondrak et al., 2008). This model satisfactorily reproduces the PO and Ca ablation profiles observed in the MASI, correctly predicting that meteoritic P is moderately volatile (similar to Fe) compared with the more refractory Ca. The speciation of ablated P is sensitive to the oxygen fugacity, and P should mainly be injected into the Earth's atmosphere as OPO, which then likely undergoes dissociation to PO (and perhaps to P and P^+), through hyperthermal collisions with air molecules. The global input of ablated P to the atmosphere was estimated to be 6,200 kg yr^{-1} (Carrillo-Sánchez, Bones, et al., 2020).

The vaporized phosphorus species will then undergo chemical processing to form a variety of compounds in which P may exist in different oxidation states due to the presence of both oxidizing and reducing agents in the upper atmosphere. In Section 2 of this paper, we develop a network of P atmospheric chemistry reactions. This involves combining our recent laboratory kinetic studies of the reactions of P, PO, and OPO (Douglas et al., 2019, 2020) with theoretical estimates of the rate coefficients of reactions not yet studied experimentally; these are determined using high-level electronic structure calculations to determine energetically viable reaction pathways and then applying statistical rate theory. In Section 3, the P chemical network is incorporated into a global chemistry-climate model. As discussed in Section 4, the model results indicate that in the present-day atmosphere about 11% of the P entering the atmosphere should be deposited at the surface in the reduced form of biologically active metal phosphites.

2. Phosphorus Atmospheric Chemistry

Figure 1 is a schematic diagram of the likely chemical pathways from P to either phosphonic (P oxidation state 3) or phosphoric acid (P oxidation state 5). This scheme has been constructed from laboratory rate coefficient measurements, and then using theoretical techniques described below to elucidate likely reaction pathways involving the reactants available in the upper mesosphere and lower thermosphere (MLT) region, such as O_3, O, O_2, H, H_2O, CO_2, NO^+, O_2^+, and electrons (Plane et al., 2015). The rate coefficients for the reactions shown in Figure 1 are listed in Table 1.

For the neutral reactions discussed in Section 2.1, electronic structure calculations were carried out using the Gaussian 16 suite of programs (Frisch et al., 2016) to determine the nature of the potential energy surface (PES). The vibrational frequencies, rotational constants, and energies of the stationary points (i.e., reactants, intermediates, transition states, and products) of each reaction were calculated with the Complete Basis Set (CBS-QB3) method (Montgomery et al., 1999). Tables S1–S9 list the Cartesian coordinates, molecular parameters, and heats of formation of the relevant neutral phosphorus species.

Rice-Ramsperger-Kassel-Markus (RRKM) calculations were then performed for each reaction using the Master Equation Solver for Multi-Energy well Reactions program (Glowacki et al., 2012). Each reaction is assumed to proceed through the formation of an excited adduct, which can either dissociate or be stabilized by collision with the N_2 third body. The internal energy of this adduct was divided into a contiguous set of grains (typical width 50 cm^{-1}) containing a bundle of rovibrational states. Each grain was then assigned

Table 1
Phosphorus Chemistry in the Mesosphere and Lower Thermosphere

No.	Reaction	Rate coefficient[a]
Neutral reactions		
R1	$P + O_2 \rightarrow PO + O$	$k_1 = 3.08 \times 10^{-13} (T/298)^{2.24}$[b]
R2	$PO + O_2 \rightarrow OPO + O$	$k_2 = 1.42 \times 10^{-11} (T/298)^{0.305}$[b]
R3	$OPO + O_3 \rightarrow PO_3 + O_2$	$k_3 = 3.72 \times 10^{-11} \exp(-1{,}131/T)$[c]
R4	$PO_3 + O \rightarrow OPO + O_2$	$k_4 = 4.01 \times 10^{-11} (T/298)^{-0.04}$[d]
R5	$PO_3 + H \rightarrow OPO + OH$	$k_5 = 2 \times 10^{-10} (T/298)^{0.5}$[e]
R6a	$OPO + H (+N_2) \rightarrow HPO_2$	$k_{6a} = 2.01 \times 10^{-28} (T/298)^{-2.31}$[d]
R6b	$OPO + H (+N_2) \rightarrow HOPO$	$k_{6b} = 1.26 \times 10^{-27} (T/298)^{-2.93}$[d]
R7	$HPO_2 + H_2O (+N_2) \rightarrow H_3PO_3$	$k_7 = 5.09 \times 10^{-28} (T/298)^{0.883}$[d]
R8	$OPO + OH (+N_2) \rightarrow HOPO_2$	$k_8 = 5.63 \times 10^{-27} (T/298)^{-3.56}$[d]
R9	$HOPO + OH \rightarrow HOPO_2 + H$	$k_9 = 6.21 \times 10^{-11} (T/298)^{-1.25}$[d]
R10a	$HPO_2 + OH \rightarrow HOPO_2 + H$	$k_{10a} = 8.81 \times 10^{-11} (T/298)^{0.010}$[d]
R10b	$HPO_2 + OH \rightarrow HOPO + OH$	$k_{10b} = 8.96 \times 10^{-12} (T/298)^{0.363}$[d]
R11	$HOPO_2 + H_2O (+N_2) \rightarrow H_3PO_4$	$\log_{10}(k_{11}) = -13.290 - 10.378 \log_{10}(T) + 1.9723(\log_{10}(T))^2$[d]
R12	$HOPO_2 + H (+N_2) \rightarrow OP(OH)_2$	$k_{12} = 5.85 \times 10^{-25} (T/298)^{0.358}$[d]
R13	$OP(OH)_2 + OH (+N_2) \rightarrow H_3PO_4$	$\log_{10}(k_{13}) = -36.906 + 23.3622 \log_{10}(T) - 4.9468 (\log_{10}(T))^2$[d]
R14	$HPO_2 + H \rightarrow OPO + H_2$	$k_{14} = 5.42 \times 10^{-11} \exp(-1{,}548/T)$[d]
R15	$HOPO + H (+N_2) \rightarrow HP(O)OH$	$k_{15} = 1.22 \times 10^{-28} (T/298)^{-3.13}$[d]
R16	$OP(OH)_2 + H \rightarrow HOPO_2 + H_2$	$k_{16} = 2 \times 10^{-10} (T/298)^{0.5}$[e]
R17	$OP(OH)_2 + O \rightarrow HOPO_2 + OH$	$k_{17} = 2 \times 10^{-10} (T/298)^{0.5}$[e]
R18	$HP(O)OH + H \rightarrow HOPO + H_2$	$k_{18} = 2 \times 10^{-10} (T/298)^{0.5}$[e]
R19a	$HP(O)OH + O \rightarrow OPO + H_2O$	$k_{19a} = 1.20 \times 10^{-10} (T/298)^{0.125}$[d]
R19b	$HP(O)OH + O \rightarrow HOPO_2 + H$	$k_{19b} = 2.94 \times 10^{-11} (T/298)^{-0.028}$[d]
R19c	$HP(O)OH + O \rightarrow HPO_2 + OH$	$k_{19c} = 1.90 \times 10^{-11} (T/298)^{-0.018}$[d]
R19d	$HP(O)OH + O \rightarrow HOPO + OH$	$k_{19d} = 1.73 \times 10^{-11} (T/298)^{-0.08}$[d]
R20	$HP(O)OH + OH \rightarrow HOPO + H_2O$	$k_{20} = 2 \times 10^{-10} (T/298)^{0.5}$[e]
Ion-molecule reactions		
R21	$P^+ + O_2 \rightarrow PO^+ + O$	$k_{21} = 5.30 \times 10^{-10}$[f]
R22	$P^+ + CO_2 \rightarrow PO^+ + CO$	$k_{22} = 4.90 \times 10^{-10}$[f]
R23	$P + O_2^+ \rightarrow P^+ + O_2$	$k_{23} = 1 \times 10^{-9}$[g]
R24	$PO + NO^+ \rightarrow PO^+ + NO$	$k_{24} = 1 \times 10^{-9}$[g]
R25	$PO + O_2^+ \rightarrow PO^+ + O_2$	$k_{25} = 1 \times 10^{-9}$[g]
R26	$OPO + O_2^+ \rightarrow OPO^+ + O_2$	$k_{26} = 1 \times 10^{-9}$[g]
R27	$OPO^+ + O \rightarrow PO^+ + O_2$	$k_{27} = 3 \times 10^{-10}$[g]
R28	$OPO^+ + e^- \rightarrow PO + O$	$k_{28} = 3 \times 10^{-7} (T/298)^{-0.5}$[h]
R29	$PO^+ + e^- \rightarrow P + O$	$k_{29} = 3 \times 10^{-7} (T/298)^{-0.5}$[h]
Photochemical reactions		
R30	$HOPO + h\nu \rightarrow H + OPO$	$J_{30} = 2.8 \times 10^{-3}$[i]
R31	$HPO_2 + h\nu \rightarrow H + OPO$	$J_{31} = 5.0 \times 10^{-5}$[i]
R32	$H_3PO_3 + h\nu \rightarrow OP(OH)_2 + H$	$J_{32} = 5.0 \times 10^{-6}$[i]
R33	$H_3PO_4 + h\nu \rightarrow OP(OH)_2 + OH$	$J_{33} = 1.4 \times 10^{-5}$[i]
R34	$HOPO_2 + h\nu \rightarrow OH + OPO$	$J_{34} = 6.1 \times 10^{-5}$[i]
Condensation reactions		
R35	$H_3PO_3 + FeOH \rightarrow MSP\text{-}PO_3$	$k_{35} = 1 \times 10^{-9}$[j]
R36	$H_3PO_3 + Fe(OH)_2 \rightarrow MSP\text{-}PO_3$	$k_{36} = 1 \times 10^{-9}$[j]
R37	$H_3PO_4 + FeOH \rightarrow MSP\text{-}PO_4$	$k_{37} = 1 \times 10^{-9}$[j]
R38	$H_3PO_4 + Fe(OH)_2 \rightarrow MSP\text{-}PO_4$	$k_{38} = 1 \times 10^{-9}$[j]

[a]Units: s^{-1} for photolysis reactions; cm^3 molecule^{-1} s^{-1} for bimolecular reactions; cm^6 molecule^{-2} s^{-1} for termolecular reactions. [b]Douglas et al.(2019). [c]Douglas et al.(2020). [d]RRKM Master Equation calculation (see text). [e]Set to a typical collision frequency, since the reaction is barrierless. [f]Anicich(2003). [g]Set to a typical value for charge exchange with these molecular ions (Plane et al., 2015). [h]Set to a typical value for the dissociative recombination of a small molecular ion with an electron (Florescu-Mitchell & Mitchell, 2006). [i]Calculated at the TD//B3LYP/6–311 + g(2d,p) level of theory (see text). [j]See text.

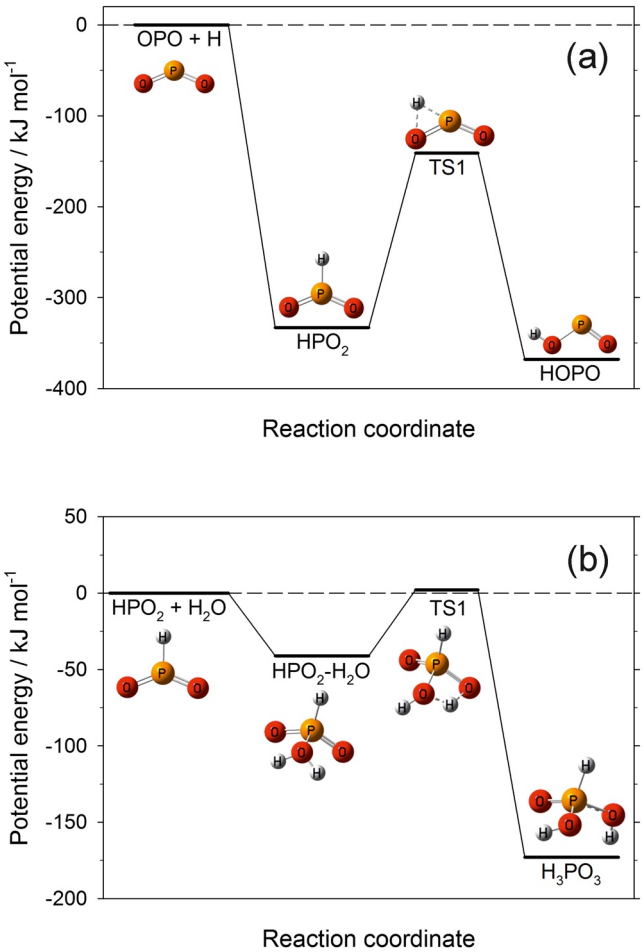

Figure 2. Potential energy surfaces calculated at the CBS-QB3 level of the theory (Montgomery et al., 1999): (a) OPO + H forming HPO_2 or HOPO; (b) HPO_2 recombining with H_2O to form H_3PO_3 (phosphonic acid).

a set of microcanonical rate coefficients for dissociation to reactants or products (where appropriate). These were determined using inverse Laplace transformation to link them directly to $k_{rec,\infty}$, the high pressure limiting recombination coefficient for the forward or reverse reaction. $k_{rec,\infty}$ was set to 5×10^{-10} $(T/300)^{0.167}$ cm^3 molecule^{-1} s^{-1}, typical of the capture rate coefficient for a reaction governed by long-range dispersive and dipole-induced dipole forces (Georgievskii & Klippenstein, 2005). The density of states of each adduct was calculated with the vibrational frequencies and rotational constants listed in Tables S1–S9, without making a correction for anharmonicity, and a classical densities of states treatment for the rotational modes. The microcanonical rate coefficients for reactions over barriers were treated using RRKM theory, with Eckart tunneling applied where an H atom transfer occurred (Glowacki et al., 2012). The probability of collisional transfer between grains following collision with air molecules (treated here as N_2) was estimated using the exponential down model; the average energy for downward transitions, $\langle \Delta E \rangle_{down}$, was set to 300 cm^{-1} at 300 K with a small $T^{0.25}$ temperature dependence, and the probabilities for upward transitions determined by detailed balance (Gilbert & Smith, 1990). The collision rate of N_2 with the adduct as a function of temperature was calculated using Lennard-Jones parameters (σ = 3.0 Å and ε = 200 cm^{-1}) to characterize the intermolecular potential. The Master Equation (which describes the evolution with time of the adduct grain populations) was then expressed in matrix form and solved to yield the rates of the various possible reaction channels (i.e., recombination and/or bimolecular reaction), at a specified pressure and temperature.

2.1. Neutral Chemistry

The initial oxidation of P will proceed through the successive oxidation by O_2 to produce OPO (reactions R1 and R2 below) (Douglas et al., 2019, 2020). O_3 probably also plays an analogous role to O_2 in oxidizing P to OPO, but the O_3/O_2 ratio in the MLT is only around 10^{-5} so its role will be very minor. OPO can then be oxidized to PO_3 by the very exothermic reaction with O_3 (R3) (Douglas et al., 2020). However, PO_3 is reduced back to OPO by reaction with O and H (R4 and R5). There is a submerged barrier on the PO_3 + O PES (87 kJ mol^{-1} below the reactants—see Table S5). This reaction should therefore proceed close to the collision frequency between PO_3 and O, divided by a statistical factor of 2 to take account of the fact that only the PES of doublet spin multiplicity is reactive (the reaction involves reactants with doublet (PO_3) and triplet (O) spin multiplicities and can therefore proceed on surfaces of doublet or quartet multiplicity). There is no barrier on the PO_3 + H PES.

	$\Delta H^\circ_{(0\,K)}$ (kJ mol^{-1})	
$P + O_2 \rightarrow PO + O$	− 100	(R1)
$PO + O_2 \rightarrow OPO + O$	− 12	(R2)
$OPO + O_3 \rightarrow PO_3 + O_2$	− 305	(R3)
$PO_3 + O \rightarrow OPO + O_2$	− 93	(R4)
$PO_3 + H \rightarrow OPO + OH$	− 22	(R5)

In the MLT, OPO is therefore likely to recombine with H to form either HPO_2 or HOPO (R6a or R6b), on the PES illustrated in Figure 2. R6a is the slightly less exothermic channel, and so 11% of the product is predicted to be HPO_2 at 200 K (a temperature typical of the MLT). As shown by the green arrows in Figure 1,

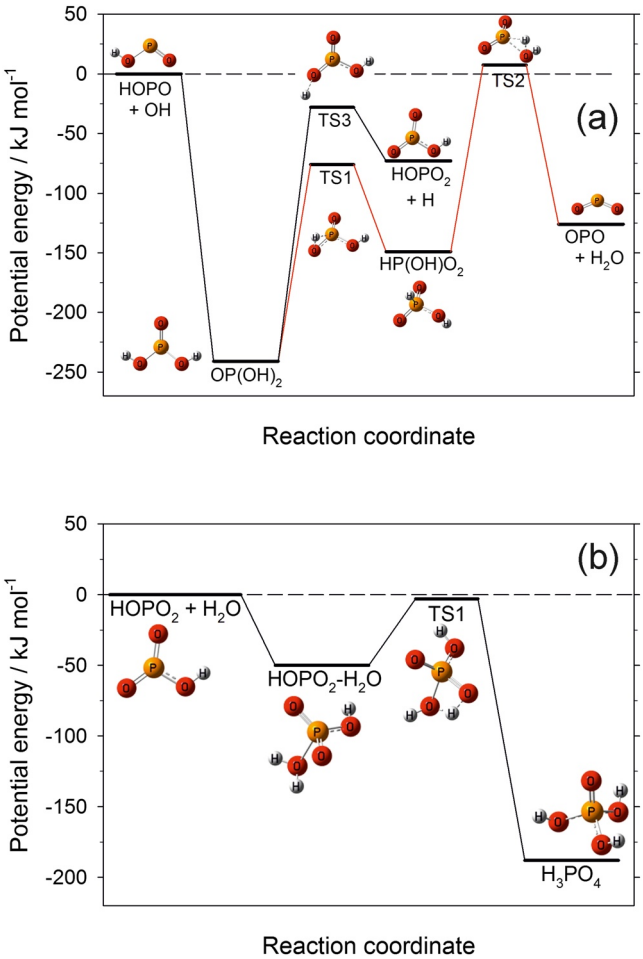

Figure 3. Potential energy surfaces calculated at the CBS-QB3 level of the theory (Montgomery et al., 1999): (a) HOPO + OH to form $HOPO_2$ (black route) or OPO + H_2O (red route) and (b) $HOPO_2$ recombining with H_2O to form H_3PO_4 (phosphoric acid).

the route to H_3PO_3 (phosphonic acid) then requires the recombination of HPO_2 with H_2O (R7), on the PES illustrated in Figure 2b. This reaction involves formation of an HPO_2–H_2O complex, which then rearranges over an essentially thermoneutral barrier to H_3PO_3.

H_3PO_4 (phosphoric acid) is formed through $HOPO_2$, the P-analog of nitric acid (major pathways depicted with red arrows in Figure 1). $HOPO_2$ can form by recombination of OPO with OH (R8). However, the more important route is through the bimolecular reaction of OH with HOPO (R9). The PES for this reaction, illustrated in Figure 3a, shows that the alternative pathway to OPO + H_2O involves a barrier of 8 kJ mol^{-1}. $HOPO_2$ can also form through the reaction of HPO_2 with OH (R10a). The PES for R10 is shown in Figure S1. The reaction channel forming HOPO is minor (8% at 200 K), and OPO formation is insignificant. H_3PO_4 then forms by the recombination of $HOPO_2$ with H_2O (R11). The PES for this reaction (Figure 3b) shows that the formation of a $HOPO_2$-H_2O complex is followed by rearrangement over a thermoneutral barrier to H_3PO_4. Alternatively, H_3PO_4 can form by the sequential addition of H and OH (R12 and R13), though this is a less important route (see Section 4).

	$\Delta H^\circ_{(0\,K)}$ (kJ mol^{-1})	
$OPO + H(+M) \rightarrow HPO_2$	− 333	(R6a)
$OPO + H(+M) \rightarrow HOPO$	− 368	(R6b)
$HPO_2 + H_2O(+M) \rightarrow H_3PO_3$	− 173	(R7)
$OPO + OH(+M) \rightarrow HOPO_2$	− 441	(R8)
$HOPO + OH \rightarrow HOPO_2 + H$	− 73	(R9)
$HPO_2 + OH \rightarrow HOPO_2 + H$	− 108	(R10a)
$HOPO_2 + H_2O(+M) \rightarrow H_3PO_4$	− 188	(R11)
$HOPO_2 + H(+M) \rightarrow OP(OH)_2$	− 167	(R12)
$OP(OH)_2 + OH(+M) \rightarrow H_3PO_4$	− 514	(R13)

Other reactions, which cycle between $OP(OH)_2$, HP(O)OH, $HOPO_2$, HOPO, and HPO_2 are illustrated in Figure 1, and their rate coefficients are listed in Table 1 (R14–R20). These reactions involve the species O, H, and OH. Note that since these species have relative abundances of ~10^6:10^3:1 above 80 km (Plane et al., 2015), the OH reactions play a minor role. The PES for the reaction between HP(O)OH and O has four bimolecular reaction channels (Figure S2), though formation of OPO is the major channel (63% at 200 K).

Once H_3PO_3 and H_3PO_4 form, they appear to be stable with respect to mesospheric constituents such as H, O, and OH (their photochemistry is discussed below in Section 2.4). In the case of H_3PO_3 reacting with H, the pathway forming $OP(OH)_2$ + H_2 is exothermic by 46 kJ mol^{-1}, but has a barrier of 28 kJ mol^{-1}; and the pathway forming $HP(OH)O_2$ + H_2 is endothermic by 45 kJ mol^{-1} and has a barrier of 95 kJ mol^{-1}. The reaction of O with H_3PO_3 to form $OP(OH)_2$ + OH is exothermic by 35 kJ mol^{-1}, but has a barrier of 24 kJ mol^{-1}; the pathway forming $HP(OH)O_2$ + OH is endothermic by 56 kJ mol^{-1} and has a barrier of 79 kJ mol^{-1}; and although recombination of O with H_3PO_3 to form H_3PO_4 is potentially highly exothermic (by 549 kJ mol^{-1}), it would involve a non-adiabatic switch from the initial triplet surface (as well as insertion of the O into the H-P bond). The reaction of OH with H_3PO_3 to form $OP(OH)_2$ + H_2O is exothermic by 102 kJ mol^{-1}, but has a barrier of 9 kJ mol^{-1}; the pathway forming $HP(OH)O_2$ + H_2O is exothermic by 11 kJ mol^{-1} but has a barrier of 44 kJ mol^{-1}; and the reaction to form H_3PO_4 + H is exothermic by 123 kJ mol^{-1} but has a barrier of 20 kJ mol^{-1}. Since there does not appear to be a low temperature route to form $HP(OH)O_2$ from H_3PO_3, $HP(OH)O_2$ is not shown in Figure 1.

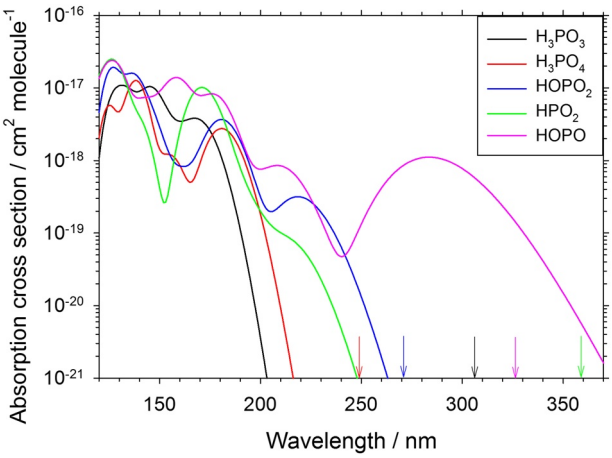

Figure 4. Absorption cross sections of H_3PO_3, H_3PO_4, $HOPO_2$, HPO_2, and HOPO computed at the TD//B3LYP/6–311 + g(2d,p) level of theory (Frisch et al., 2016). The vertical arrows indicate upper limits to the photolysis thresholds, computed from the relevant bond dissociation energies at the CBS-QB3 level of theory (Montgomery et al., 1999).

In the case of H_3PO_4, reaction with H to form $OP(OH)_2 + H_2O$ and $OP(OH)_2O + H_2$ is endothermic by 21 and 45 kJ mol^{-1}, respectively; reaction with OH to form $OP(OH)_2O + H_2O$ is exothermic by 12 kJ mol^{-1} but has a barrier of 24 kJ mol^{-1}; and reaction with O to form $H_3PO_3 + O_2$ is endothermic by 52 kJ mol^{-1}. HP(OH)O is therefore omitted from Figure 1.

2.2. Ion-Molecule Chemistry

The ion-molecule chemistry of phosphorus is comparatively unimportant. This is because P^+ ions react rapidly with O_2 (and CO_2, R22) to produce PO^+ (R21) (Anicich, 2003). This reaction is highly exothermic even if the O is produced in the singlet excited state to conserve spin on a singlet surface:

$$P^+ + O_2 \rightarrow PO^+ + O(^1D) \quad \Delta H^\circ_{(0\,K)} = -111\,\text{kJ mol}^{-1} \qquad \text{(R21)}$$

P-containing ions can be formed either directly during ablation (Carrillo-Sánchez, Bones, et al., 2020) or through exothermic charge transfer reactions (R23–R26) between P, PO, and OPO and the ambient ions NO^+ and O_2^+ in the lower *E* region (90–150 km). Note that the reaction between P and O_2^+ could also make $PO^+ + O$ directly (exothermic by 453 kJ mol^{-1}), though P should be a very minor species because the rate of R1 is so high. OPO^+ can be reduced back to PO^+ by O:

$$OPO^+ + O \rightarrow PO^+ + O_2 \quad \Delta H^\circ_{(0\,K)} = -218\,\text{kJ mol}^{-1} \qquad \text{(R27)}$$

However, the reaction of PO^+ with O is very endothermic (by 301 kJ mol^{-1} or 395 kJ mol^{-1}, if spin is conserved to produce $P^+ + O_2(a^1\Delta_g)$). In contrast, the meteor-ablated metallic ions such as Fe^+ and Mg^+ can only form their comparatively weakly bound oxides FeO^+ and MgO^+ by reaction with O_3 rather than O_2, and these oxides are very rapidly reduced back to the atomic ions by reaction with the large excess of O in the lower thermosphere (Plane et al., 2015). Atomic ions can only be neutralized by the relatively slow process of dielectronic (or radiative) recombination with electrons, which allows significant concentrations of metallic atomic ions to occur above 90 km in the atmosphere (Plane et al., 2015). In contrast, molecular ions such as PO^+ and OPO^+ will undergo much faster dissociative recombination reactions (R28 and R29), and the concentrations of these ions should be relatively small in the MLT.

2.3. Photochemistry

The photolysis rates of H_3PO_3, H_3PO_4, $HOPO_2$, HPO_2, and HOPO were estimated by using time-dependent density function theory (TD-DFT) (Bauernschmitt & Ahlrichs, 1996). The vertical excitation energies and transition dipole moments for transitions from the ground state of each molecule up to the first 30 electronically excited states were calculated to produce the absorption cross sections shown in Figure 4. Each cross section was then convolved up to its dissociation threshold with the solar actinic flux from the SOLAR2000 empirical solar irradiance model (Tobiska et al., 2000) (averaged over a solar cycle). The resulting photodissociation reactions are shown in Table 1 (R30–R34). The photolysis threshold was set to correspond to the lowest bond dissociation energy at the CBS-QB3 level of theory. These thresholds, indicated with arrows in Figure 4, are an upper wavelength limit because a photon with more than the bond energy may be required depending on the position of the upper dissociating electronic states.

Figure 4 shows that the absorption cross section of H_3PO_3 (black line) only starts to become significant below 200 nm, and so it has the lowest photodissociation rate of 5.0×10^{-6} s^{-1}. HOPO, in contrast, can potentially photolyze below 327 nm where it already has a large absorption cross section, and so its photodissociation rate is estimated to be 2.8×10^{-3} s^{-1} (Table 1).

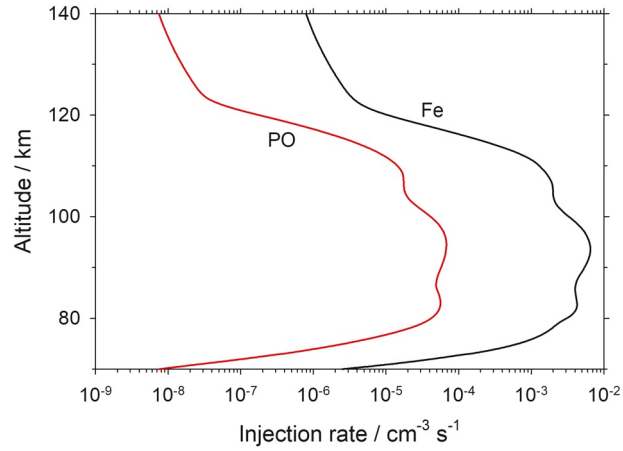

Figure 5. Global annual mean injection rates of PO (representing P + PO + OPO) and Fe from meteoric ablation. The injection profiles predicted by the CABMOD-ZoDY model (Carrillo-Sánchez, Bones, et al., 2020; Carrillo-Sánchez, Gómez-Martín, et al., 2020) have been divided by a factor of 5.0 for input into the WACCM6 model (see text).

2.4. Incorporation Into Meteoric Smoke Particles

Reactions R35–R38 in Table 1 are condensation reactions (i.e., acid + base→salt + H_2O) of H_3PO_3 and H_3PO_4 with alkaline metal-containing molecules represented here as FeOH and $Fe(OH)_2$, which are reservoir species for meteor-ablated Fe below the atomic Fe layer centered around 86 km (Feng et al., 2013). Fe is the most abundant meteoric metal, followed by Mg and Na. Their major molecular reservoirs (Plane et al., 2015) all undergo exothermic condensation reactions with the acidic H_3PO_3 and H_3PO_4:

	$\Delta H^\circ_{(0\,\mathrm{K})}\left(\mathrm{kJ\ mol^{-1}}\right)$
$FeOH + H_3PO_3 \rightarrow FeH_2PO_3 + H_2O$	−103
$Fe(OH)_2 + H_3PO_3 \rightarrow HOFeH_2PO_3 + H_2O$	−114
$MgOH + H_3PO_3 \rightarrow MgH_2PO_3 + H_2O$	−120
$Mg(OH)_2 + H_3PO_3 \rightarrow HOMgH_2PO_3 + H_2O$	−132
$NaHCO_3 + H_3PO_3 \rightarrow NaH_2PO_3 + H_2O + CO_2$	−79
$FeOH + H_3PO_4 \rightarrow FeH_2PO_4 + H_2O$	−70
$Fe(OH)_2 + H_3PO_4 \rightarrow HOFeH_2PO_4 + H_2O$	−111
$MgOH + H_3PO_4 \rightarrow MgH_2PO_4 + H_2O$	−119
$Mg(OH)_2 + H_3PO_4 \rightarrow HOMgH_2PO_4 + H_2O$	−129
$NaHCO_3 + H_3PO_4 \rightarrow NaH_2PO_4 + H_2O + CO_2$	−74

The resulting metal phosphite and phosphate molecules are illustrated in Figure S3. As shown in Table 1, the rate coefficients k_{35}–k_{38} are set to 1×10^{-9} cm^3 molecule^{-1} s^{-1}. This represents a typical rate coefficient of 5×10^{-10} cm^3 molecule^{-1} s^{-1} for long-range capture involving molecules with permanent dipole moments (hence the absence of a significant temperature dependence) (Georgievskii & Klippenstein, 2005), multiplied by a factor of 2 to take account of the fact that Fe is ∼48% of the total ablated meteoric metals (≈Fe + Mg + Na) (Carrillo-Sánchez, Gómez-Martín, et al., 2020). The metal phosphites/phosphates produced by R35–R38 are assumed to be phosphorus sinks, and these become incorporated into meteoric smoke particles (MSPs), the nm-sized particles, which form in the MLT from the polymerization of meteoric metal compounds (Plane et al., 2015).

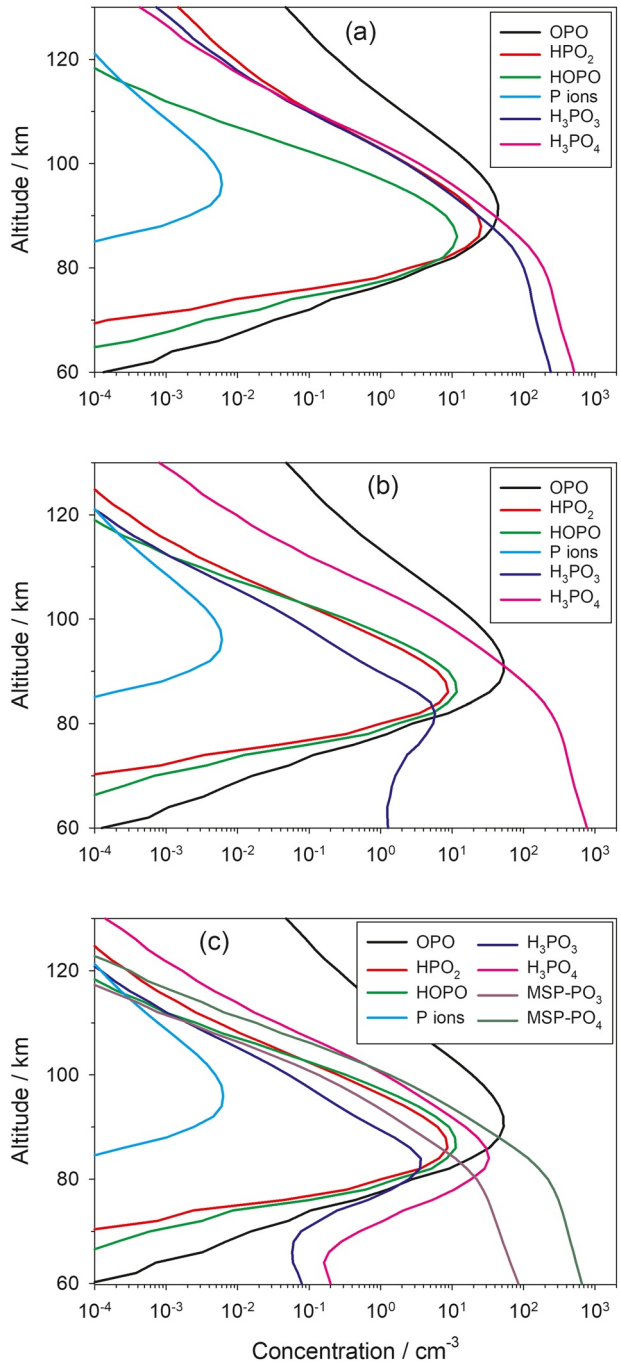

Figure 6. Mean vertical profiles of P-containing species averaged over 11 years (2004–2014) at midlatitudes (54°N): (a) photolysis of P species (R34–R38) turned off and meteoric smoke particle (MSP)-forming condensation reactions (R30–R33) turned off; (b) photolysis (R34–R38) turned on, MSP formation (R30–R33) turned off; (c) photolysis and MSP formation turned on (i.e., full P chemistry R1–R38 turned on).

3. Global Modeling of Phosphorus in the MLT Region

3.1. WACCM-P Set Up

The phosphorus reactions in Table 1 were imported into the Whole Atmosphere Community Climate Model (WACCM) (Gettelman et al., 2019) from the US National Center for Atmospheric Research. We have previously used this global chemistry-climate model to study the atmospheric chemistries of various meteor-ablated metals, including Fe (Feng et al., 2013), Mg (Langowski et al., 2015), and Na (Marsh et al., 2013). The version we employ here, WACCM6 (Gettelman et al., 2019), uses the framework developed from the second iteration of the fully coupled Community Earth System Model (CESM2) (Danabasoglu et al., 2020). The model extends vertically from the surface to the lower thermosphere at ~140 km. In the present study, we used the free-running (FR) version of WACCM because there are no observations of P species against which to compare the simulations (and the FR version simulates Fe and Fe^+ satisfactorily [Feng et al., 2013]). The model has a horizontal resolution of 1.9° latitude × 2.5° longitude, and 70 vertical model layers (~3.5 km vertical resolution in the MLT region). This version of WACCM6 with phosphorus chemistry is termed here as WACCM-P. The full set of Fe reactions in WACCM-Fe (Feng et al., 2013; Viehl et al., 2016) was also included in order to produce the FeOH and $Fe(OH)_2$ required for R35–R38. The model simulations were performed from 2004 to 2014 using the standard WACCM6 initialization conditions file (Danabasoglu et al., 2020), following a 5-year spin-up with Fe and P chemistry. This 11-year period is sufficiently long to produce a climatology of the phosphorus species.

3.2. The Phosphorus Meteoric Input Function

Figure 5 shows the global average injection profiles of PO and Fe used in WACCM. Note that although ~6 times more OPO than PO should ablate (Carrillo-Sánchez, Bones, et al., 2020), most of the OPO will then be converted immediately to PO through hyperthermal collisions with N_2 or O_2. The PO profile shown here is therefore the total phosphorus input. These meteoric input functions (MIFs) were estimated by combining the new version of the Chemical ABLation MODel (CABMOD-3), which simulates the ablation of the major meteoric elements and OPO/PO/P from an individual dust particle (Carrillo-Sánchez, Bones, et al., 2020; Carrillo-Sánchez, Gómez-Martín, et al., 2020), with the Zodiacal Cloud Model (ZoDY), which provides the mass, velocity, and radiant distributions of particles entering the atmosphere. ZoDY contains contributions from different dust sources: Jupiter Family Comets, the asteroid belt, and long-period Halley-Type comets (Nesvorný et al., 2011), which are weighted using the procedure described in Carrillo-Sánchez et al. (2016). The PO and Fe injection height profiles in Figure 5 are similar in shape, peaking around 94 km. The ratio of the PO:Fe injection rates is ~0.01 between 70 and 140 km, which is close to their relative elemental abundance in meteorites of 9.6×10^{-3} (Asplund et al., 2009) multiplied by their relative ablation efficiency of 1.13 (Carrillo-Sánchez, Bones, et al., 2020). The secondary peak around 108 km in both injection profiles arises from fast meteors (mostly from Halley-Type comets), and the lower peaks from slow meteors (mostly from Jupiter Family comets and asteroidal particles).

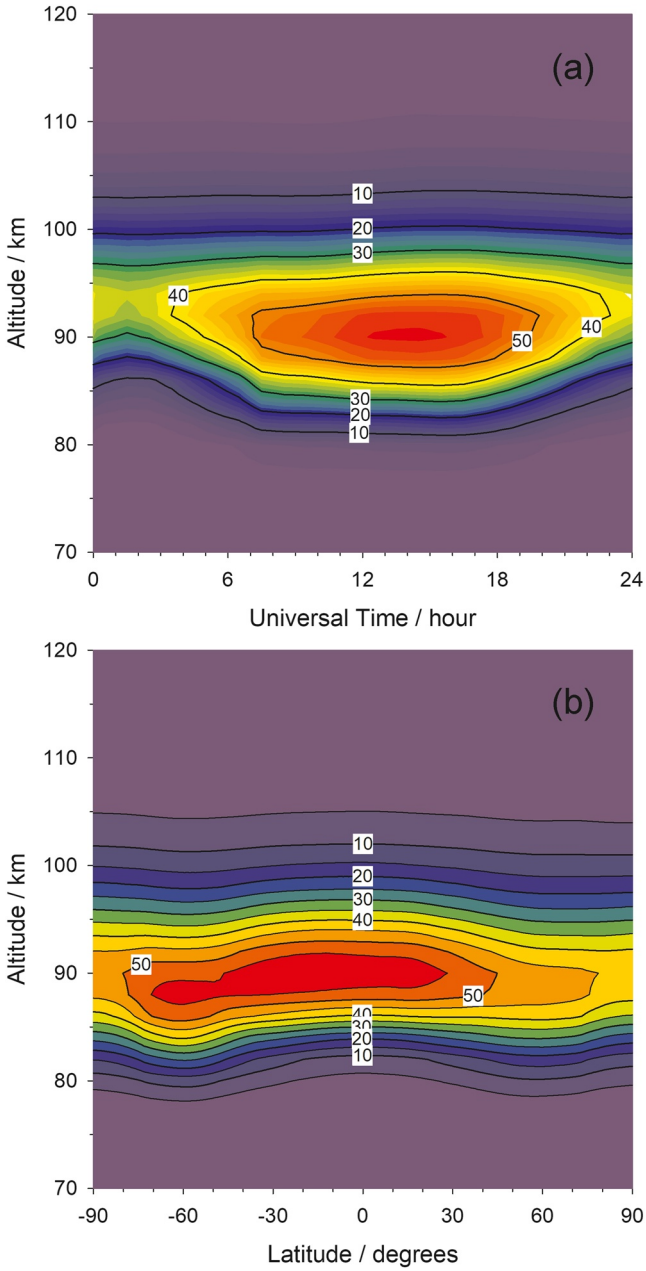

Figure 7. (a) Diurnal variation of OPO density (molecule cm^{-3}) as a function of altitude at the location 54°N 12°E, computed from hourly model output. (b) Zonally averaged OPO density as a function of latitude and height, computed from monthly mean (diurnally averaged) output. The data are averaged over 11 years (2004–2014).

The PO and Fe injection profiles in Figure 5 have been reduced by a factor of 5 from the profiles predicted by the CABMOD-ZoDY model (Carrillo-Sánchez, Bones, et al., 2020; Carrillo-Sánchez, Gómez-Martín, et al., 2020). This is a standard procedure that we have adopted to allow for the fact that vertical transport of minor species in the MLT tends to be underestimated in global models such as WACCM6 (Daly et al., 2020; Plane et al., 2018). The "missing" transport arises because short wavelength gravity waves are not resolved on the current horizontal grid scale of the model (~220 km), and these sub-grid waves contribute to vertical chemical and dynamical transport of constituents while dissipating (Gardner et al., 2017). In order to correctly simulate the observed *absolute* densities of species such as Fe, Na, and Ca when vertical transport is underestimated, the MIF of each species needs to be reduced by this factor of ~5 (Daly et al., 2020; Plane et al., 2018). The PO MIF is then set to vary with season and latitude in the same way as the Fe MIF (Feng et al., 2013), that is, an autumnal maximum and vernal minimum, increasing from essentially no variation at the equator to ±30% at the pole, with the same annual average input at all latitudes.

4. Discussion

Figure 6 illustrates the results of three WACCM-P runs, which explore the role of photolysis and MSP formation. The panels show the vertical profiles of the P-containing species, averaged over 11 years (2004–2014) at midlatitudes (54°N). For all three model experiments, the P ions are very minor species, occurring in a layer that peaks around 95 km with a peak concentration of only 7×10^{-2} cm^{-3}. This result was anticipated in Section 3.2: P^+ ions are overwhelmingly converted to molecular PO^+ by reaction with O_2 or CO_2, and PO^+ then undergoes rapid dissociative recombination with electrons. This is consistent with the absence of P^+ in rocket-borne mass spectrometric measurements in the Earth's lower *E* region (Grebowsky & Aikin, 2002; Kopp et al., 1985), and measurements with the Neutral Gas Ion Mass Spectrometer instrument on the MAVEN satellite orbiting Mars, where the atomic ions of less abundant meteoric species (e.g., K^+, Ti^+, and Cu^+) were observed (Benna et al., 2015).

The three panels in Figure 6 show that above 90 km the major P-containing species is OPO, which occurs in a broad layer peaking around 90 km, with a full width at half maximum (FWHM) of ~14 km. HPO_2 and HOPO also occur in layers which peak around 86 km, since they are produced by the pressure-dependent recombination of OPO with H (R6a and b). P, PO, $HOPO_2$, and PO_3 are very minor, with a combined total concentration of less than 0.02 cm^{-3}.

The only other important neutral species are H_3PO_3 and H_3PO_4. In Figure 6a where there is no photolysis or MSP formation, they become the dominant species below 86 km since they represent the two phosphorus sinks (Figure 1). The H_3PO_3:H_3PO_4 ratio is ~0.5 below 86 km. However, when photolysis is turned on (Figure 6b), H_3PO_3 is significantly depleted and the ratio becomes less than 0.01. The reason for this is that, although the H_3PO_3 photodissociation rate is relatively small (Section 2.3), the lowest energy dissociation channel of H_3PO_3 produces $OP(OH)_2$ + H (R32), and $OP(OH)_2$ can then form H_3PO_4 (Figure 1). It should be kept in mind that the production of $OP(OH)_2$ from H_3PO_3 may not be the dominant photodissociation pathway: H_3PO_3 only absorbs significantly below 200 nm (Figure 4) where the photon energy is sufficient to produce $HP(OH)O_2$ + H (threshold = 482 kJ mol^{-1}, $\lambda < 248$ nm) or HP(O)OH + OH (threshold = 482 kJ mol^{-1}, $\lambda < 240$ nm).

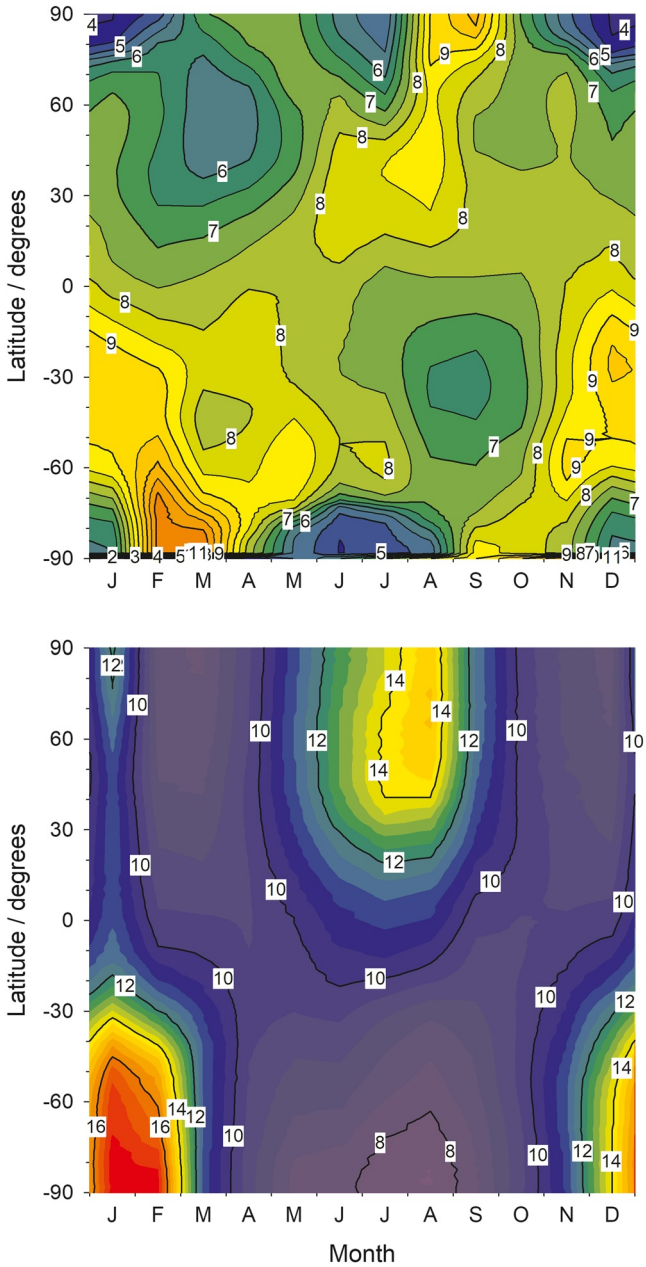

Figure 8. (a) Vertical column density (10^7 molecule cm^{-2}) of OPO as a function of latitude and season. (b) Percentage of phosphite in the vertical column of meteoric smoke particles, as a function of latitude and season. The data are averaged over 11 years (2004–2014).

Figure 6c shows the effect of including both photolysis and the condensation reactions with FeOH and $Fe(OH)_2$ to produce metal phosphites (labeled MSP-PO_3) and phosphates (MSP-PO_4). Because the total concentration of the metal hydroxides/carbonates is more than 2×10^4 cm^{-3} below 85 km (Feng et al., 2013; Marsh et al., 2013; Plane et al., 2015), the condensation reactions of H_3PO_3 and H_3PO_4 are relatively rapid and MSP-PO_3 and MSP-PO_4 become the dominant forms of phosphorus below 85 km, with a ratio of 0.10.

The OPO layer is the counterpart to the layers of metal atoms such as Na and Fe, which have been observed for decades by the ground-based lidar technique (Plane et al., 2015), and the layer of SiO that is predicted to result from the meteoric ablation of Si (Plane et al., 2016). Figure 7a illustrates the diurnal variation of the simulated OPO layer with full phosphorus chemistry (R1–R38 in Table 1) at a midlatitude site (54°N 12°E). This shows that the layer at 90 km exhibits a minimum around 0200 UT, which increases by ~90% to a maximum around 1400 UT (1448 LT). This is mostly caused by the photolysis of HOPO (in particular) and HPO_2, which prevent the formation of the more photolytically stable H_3PO_3 and H_3PO_4 (Table 1). Figure 7b illustrates the zonally averaged annual mean OPO layer as a function of latitude and month. This shows that there is modest latitudinal variation, with a 32% increase from the minimum at northern high latitudes to a maximum between 30°S and 20°N. What is striking is the clear preponderance of OPO in the Southern Hemisphere: the latitude range where the layer peak concentration is greater than 50 cm^{-3} extends to 80°S, but only to 45°N.

This hemispheric difference is explained in Figure 8a, which shows the OPO vertical column density (VCD, integrated from 64 to 130 km) versus latitude and month. The complex variation, which when averaged over the year produces the greater amount of OPO at mid-to-high southern latitudes, arises from several factors. First, the seasonal variation of the PO MIF causes the vernal minima in OPO at midlatitudes, and the autumnal maxima that extend to high latitudes in both hemispheres. Second, the minima that occur around the winter solstice at high latitudes (>65°) are caused by the absence of photochemistry during the polar night, which reduces the recycling of HOPO and HPO_2 to OPO. The mid-summer minima at high latitudes are caused by two further factors. In the upper mesosphere, there is a pronounced meridional circulation toward the winter pole (Plane et al., 2015), where convergence of the products of meteoric ablation occurs (as seen in enhanced layers of Fe and Na [Gardner et al., 2005]). The upwelling air at the summer pole causes divergence in the MLT, reducing the density of meteoric materials. Furthermore, the resulting colder temperatures favor the recombination reactions of OPO with H and OH (R6a, R6b, and R8), which have negative temperature dependences (Table 1).

OPO appears to be the only significant P-containing species, which could potentially be observed spectroscopically, using the B-X transition band between 284 and 325 nm (Douglas et al., 2020; Lei et al., 2001). The peak absorption cross section of this band is 5.7×10^{-17} cm^2 $molecule^{-1}$, calculated using the TD-DFT method with the 6–311 + g(2d,p) basis set (Bauernschmitt & Ahlrichs, 1996). For a satellite stellar or solar occultation measurement with a typical optical path through the MLT of 300 km and peak OPO concentration of 50 cm^{-3}, the optical density would be 8.4×10^{-9}. Unfortunately, this is more than 2 orders of magnitude too small to be measured with current satellite-borne spectrometers such as the GOMOS instrument on ENVISAT (Fussen et al., 2010) or the SOFIE instrument on AIM (Hervig et al., 2017).

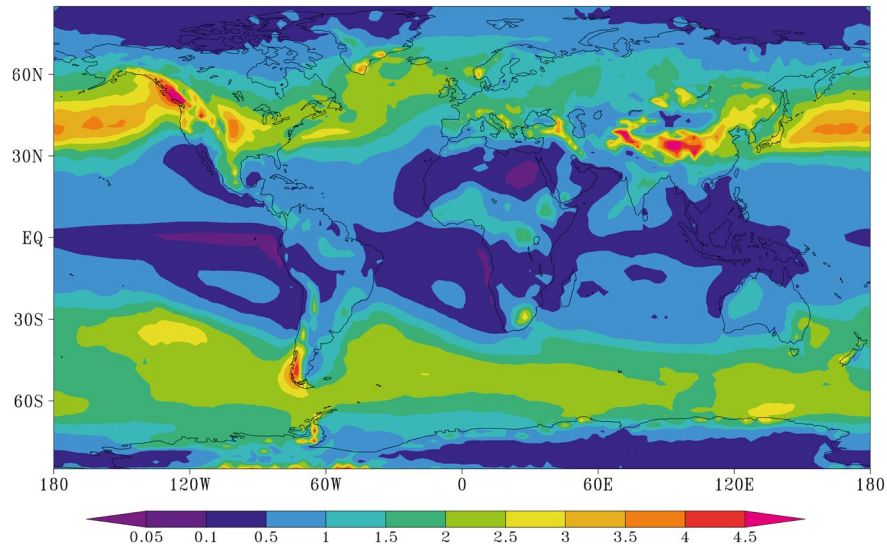

Figure 9. Map of the meteor-ablated phosphorus deposition flux (10^{-8} g m^{-2} yr^{-1}) from a 9-year run of the WACCM-CARMA model (December 2005 to November 2014). See Brooke et al. (2017) for further details.

Figure 8b shows the percentage of ablated phosphorus in the form of phosphite, as a function of latitude and month. The percentage is calculated from the VCDs of MSP-PO_3 and MSP-PO_4. The global annual average fraction of phosphite is 10.6%. However, the phosphite percentage is approximately twice as large during summer at mid- to high latitudes (>50°). Although the colder temperatures during summer would favor formation of HOPO (R6b) over HPO_2 (R6a) (see the temperatures dependences in Table 1), once HPO_2 forms, it is more likely to go on to form H_3PO_3. This is because reaction of HPO_2 with H back to OPO (R14) has a significant activation energy, and is much slower in the very cold summer upper mesosphere at high latitudes, where the typical summertime temperature is ~140 K compared with a wintertime temperature of ~220 K (Plane et al., 2015): k_{14} becomes 56 times slower. Furthermore, the H_2O concentration is ~7 times larger as upwelling air over the summer pole brings fresh H_2O from the lower mesosphere, whereas the H atom concentration only increases by a factor of 2. This makes recombination of HPO_2 with H_2O (R7) more competitive with R14.

MSPs are too small to sediment rapidly compared to being transported by the residual circulation in the middle atmosphere into the lower stratosphere, principally inside the winter polar vortex (Bardeen et al., 2008). They then enter the troposphere principally along midlatitude storm tracks, before mostly being deposited in broad bands between 40 and 60°N and 30 and 70°S (Brooke et al., 2017). Figure 9 is a world map showing the predicted deposition flux of phosphorus in MSPs. The flux is calculated from the MSP mass deposition rates reported by Brooke et al. (2017), scaled by a factor of 2.1×10^{-3} , which is the ratio of the ablated mass flux of P (Carrillo-Sánchez, Bones, et al., 2020) to the total ablated mass flux, which becomes essentially $FeMgSiO_4$ particles (Carrillo-Sánchez, Gómez-Martín, et al., 2020) (note that this ratio uses the actual P flux, rather than the flux divided by 5 for the WACCM simulations in the MLT—Section 3.2). The highest P deposition rates of around 5×10^{-8} g m^{-2} yr^{-1} are over the northern Rockies, Himalayas, and southern Andes, compared with a global mean P deposition flux of 1×10^{-8} g m^{-2} s^{-1}. The estimated phosphite deposition flux from WACCM-P is then 1×10^{-9} g m^{-2} yr^{-1}, with a maximum of 5×10^{-9} g m^{-2} yr^{-1}. This global mean flux is close to the geometric mean of the recent estimate of phosphite production from lightning strikes of between 100–10,000 kg annually (Hess et al., 2021). Moreover, the phosphate within MSPs, which are mostly less than 100 nm in radius (Bardeen et al., 2008; Brooke et al., 2017), will be even more prone to lightning-initiated reduction, or aqueous phase chemistry during their residence in the highly acidic Junge layer (Saunders et al., 2012), than the phosphate buried within much larger meteorites.

5. Conclusions

In the present study, we have developed a phosphorus chemistry network to explore possible routes from PO, OPO, and P, which ablate in the MLT from IDPs entering the Earth's atmosphere, to the stable reservoirs H_3PO_3 and H_3PO_4 which then become incorporated into MSPs as metal phosphites and phosphates, respectively. While the network is partly constructed from reactions whose kinetics have been measured experimentally, many of the critical reactions have been (necessarily) assigned theoretical rate coefficients, estimated using a combination of electronic structure theory calculations and an established RRKM master equation treatment. The estimated fraction of 11% of ablated phosphorus forming metal phosphites is of course sensitive to these estimated rate coefficients. In particular, the branching ratio to formation of HPO_2 or HOPO in the recombination of H with OPO (R6a and R6b); the recombination of H_2O with HPO_2 to form H_3PO_3 (R7); the OH reactions forming $HOPO_2$ from OPO and HOPO (R8 and R9); and the recombination of H_2O with $HOPO_2$ to form H_3PO_4 (R11).

Nevertheless, two important conclusions can be drawn. First, the ablation of phosphorus from IDPs provides a substantial and continuous source of oxidized P to the surface in the form of submicron-sized smoke particles. Second, a not insignificant fraction of the phosphorus is likely to be in the form of bioavailable phosphites rather than phosphates, because of the unusual chemical conditions in the MLT with very large concentrations of O and H compared to OH. It will be interesting to explore in future work with WACCM-P how this fraction might have changed before and during the Great Oxygenation Event in the Paleoproterozoic era, approximately 2 Gyr ago (Lyons et al., 2014).

Data Availability Statement

The model output data used in the paper are available at https://doi.org/10.5281/zenodo.5146167, and the electronic structure theory data are tabulated in Supporting Information S1.

Acknowledgments
This study was supported by funding from the UK Science and Technology Facilities Council (grant ST/P000517/1).

References

Anicich, V. G. (2003). *An index of the literature for bimolecular gas phase cation-molecule reaction kinetics* (JPL Publication 03-19). Jet Propulsion Laboratory/California Institute of Technology.

Asplund, M., Grevesse, N., Sauval, A. J., & Scott, P. (2009). The chemical composition of the sun. *Annual Review of Astronomy and Astrophysics*, *47*, 481–522. https://doi.org/10.1146/annurev.astro.46.060407.145222

Bardeen, C. G., Toon, O. B., Jensen, E. J., Marsh, D. R., & Harvey, V. L. (2008). Numerical simulations of the three-dimensional distribution of meteoric dust in the mesosphere and upper stratosphere. *Journal of Geophysical Research*, *113*, D17202. https://doi.org/10.1029/2007jd009515

Bauernschmitt, R., & Ahlrichs, R. (1996). Treatment of electronic excitations within the adiabatic approximation of time dependent density functional theory. *Chemical Physics Letters*, *256*, 454–464. https://doi.org/10.1016/0009-2614(96)00440-x

Benna, M., Mahaffy, P. R., Grebowsky, J. M., Plane, J. M. C., Yelle, R. V., & Jakosky, B. M. (2015). Metallic ions in the upper atmosphere of Mars from the passage of comet C/2013 A1 (Siding Spring). *Geophysical Research Letters*, *42*, 4670–4675. https://doi.org/10.1002/2015gl064159

Brooke, J. S. A., Feng, W. H., Carrillo-Sanchez, J. D., Mann, G. W., James, A. D., Bardeen, C. G., et al. (2017). Meteoric smoke deposition in the polar regions: A comparison of measurements with global atmospheric models. *Journal of Geophysical Research: Atmospheres*, *122*, 11112–11130. https://doi.org/10.1002/2017jd027143

Carrillo-Sánchez, J. D., Bones, D. L., Douglas, K. M., Flynn, G. J., Wirick, S., Fegley, B., et al. (2020). Injection of meteoric phosphorus into planetary atmospheres. *Planetary and Space Science*, *187*, 104926. https://doi.org/10.1016/j.pss.2020.104926

Carrillo-Sánchez, J. D., Gómez-Martín, J. C., Bones, D. L., Nesvorný, D., Pokorný, P., Benna, M., et al. (2020). Cosmic dust fluxes in the atmospheres of Earth, Mars, and Venus. *Icarus*, *335*, 113395. https://doi.org/10.1016/j.icarus.2019.113395

Carrillo-Sánchez, J. D., Nesvorný, D., Pokorný, P., Janches, D., & Plane, J. M. C. (2016). Sources of cosmic dust in the Earth's atmosphere. *Geophysical Research Letters*, *43*, 11979–11986. https://doi.org/10.1002/2016gl071697

Daly, S. M., Feng, W., Mangan, T. P., Gerding, M., & Plane, J. M. C. (2020). The meteoric Ni layer in the upper atmosphere. *Journal of Geophysical Research: Space Physics*, *125*, e2020JA028083. https://doi.org/10.1029/2020ja028083

Danabasoglu, G., Lamarque, J.-F., Bacmeister, J., Bailey, D. A., DuVivier, A. K., Edwards, J., et al. (2020). The Community Earth System Model version 2 (CESM2). *Journal of Advances in Modeling Earth Systems*, *12*, e2019MS001916. https://doi.org/10.1029/2019ms001916

Douglas, K. M., Blitz, M. A., Mangan, T. P., & Plane, J. M. C. (2019). Experimental study of the removal of ground- and excited-state phosphorus atoms by atmospherically relevant species. *The Journal of Physical Chemistry A*, *123*, 9469–9478. https://doi.org/10.1021/acs.jpca.9b07855

Douglas, K. M., Blitz, M. A., Mangan, T. P., Western, C. M., & Plane, J. M. C. (2020). Kinetic study of the reactions PO + O_2 and PO_2 + O_3 and spectroscopy of the PO radical. *The Journal of Physical Chemistry A*, *124*, 7911–7926. https://doi.org/10.1021/acs.jpca.0c06106

Feng, W., Marsh, D. R., Chipperfield, M. P., Janches, D., Höffner, J., Yi, F., & Plane, J. M. C. (2013). A global atmospheric model of meteoric iron. *Journal of Geophysical Research: Atmospheres*, *118*, 9456–9474. https://doi.org/10.1002/jgrd.50708

Florescu-Mitchell, A. I., & Mitchell, J. B. A. (2006). Dissociative recombination. *Physics Reports*, *430*, 277–374. https://doi.org/10.1016/j.physrep.2006.04.002

Frisch, M. J., Trucks, G. W., Schlegel, H. B., Scuseria, G. E., Robb, M. A., Cheeseman, J. R., et al. (2016). *Gaussian 16 Rev. B.01*.
Fussen, D., Vanhellemont, F., Tetard, C., Mateshvili, N., Dekemper, E., Loodts, N., et al. (2010). A global climatology of the mesospheric sodium layer from GOMOS data during the 2002-2008 period. *Atmospheric Chemistry and Physics*, *10*, 9225–9236. https://doi.org/10.5194/acp-10-9225-2010
Gardner, C. S., Liu, A. Z., & Guo, Y. (2017). Vertical and horizontal transport of mesospheric Na: Implications for the mass influx of cosmic dust. *Journal of Atmospheric and Solar-Terrestrial Physics*, *162*, 192–202. https://doi.org/10.1016/j.jastp.2016.07.013
Gardner, C. S., Plane, J. M. C., Pan, W., Vondrak, T., Murray, B. J., & Chu, X. (2005). Seasonal variations of the Na and Fe layers at the South Pole and their implications for the chemistry and general circulation of the polar mesosphere. *Journal of Geophysical Research*, *110*, D1030210. https://doi.org/10.1029/2004jd005670
Georgievskii, Y., & Klippenstein, S. J. (2005). Long-range transition state theory. *The Journal of Chemical Physics*, *122*, 194103. https://doi.org/10.1063/1.1899603
Gettelman, A., Mills, M. J., Kinnison, D. E., Garcia, R. R., Smith, A. K., Marsh, D. R., et al. (2019). The Whole Atmosphere Community Climate Model Version 6 (WACCM6). *Journal of Geophysical Research: Atmospheres*, *124*, 12380–12403. https://doi.org/10.1029/2019jd030943
Gibard, C., Gorrell, I. B., Jimenez, E. I., Kee, T. P., Pasek, M. A., & Krishnamurthy, R. (2019). Geochemical sources and availability of amidophosphates on the early Earth. *Angewandte Chemie International Edition*, *58*, 8151–8155. https://doi.org/10.1002/anie.201903808
Gilbert, R. G., & Smith, S. C. (1990). *Theory of unimolecular and recombination reactions*. Blackwell.
Glowacki, D. R., Liang, C. H., Morley, C., Pilling, M. J., & Robertson, S. H. (2012). MESMER: An open-source master equation solver for multi-energy well reactions. *Journal of Physical Chemistry A*, *116*, 9545–9560. https://doi.org/10.1021/jp3051033
Grebowsky, J. M., & Aikin, A. C. (2002). In situ measurements of meteoric ions. In E. Murad, & I. P. Williams (Eds.), Meteors in the Earth's atmosphere (pp. 189–214). Cambridge University Press.
Hervig, M. E., Brooke, J. S. A., Feng, W., Bardeen, C. G., & Plane, J. M. C. (2017). Constraints on meteoric smoke composition and meteoric influx using SOFIE observations with models. *Journal of Geophysical Research: Atmospheres*, *122*, 13495–13505. https://doi.org/10.1002/2017jd027657
Hess, B. L., Piazolo, S., & Harvey, J. (2021). Lightning strikes as a major facilitator of prebiotic phosphorus reduction on early Earth. *Nature Communications*, *12*, 1535. https://doi.org/10.1038/s41467-021-21849-2
Kopp, E., Eberhardt, P., Herrmann, U., & Björn, L. G. (1985). Positive ion composition of the high-latitude summer D region with noctilucent clouds. *Journal of Geophysical Research*, *90*, 13041–13053. https://doi.org/10.1029/jd090id07p13041
Langowski, M. P., von Savigny, C., Burrows, J. P., Feng, W., Plane, J. M. C., Marsh, D. R., et al. (2015). Global investigation of the Mg atom and ion layers using SCIAMACHY/Envisat observations between 70 and 150 km altitude and WACCM-Mg model results. *Atmospheric Chemistry and Physics*, *15*, 273–295. https://doi.org/10.5194/acp-15-273-2015
Lei, J., Teslja, A., Nizamov, B., & Dagdigian, P. J. (2001). Free-jet electronic spectroscopy of the PO_2 radical. *The Journal of Physical Chemistry A*, *105*, 7828–7833. https://doi.org/10.1021/jp011778p
Lyons, T. W., Reinhard, C. T., & Planavsky, N. J. (2014). The rise of oxygen in Earth's early ocean and atmosphere. *Nature*, *506*, 307–315. https://doi.org/10.1038/nature13068
Maciá, E. (2005). The role of phosphorus in chemical evolution. *Chemical Society Reviews*, *34*, 691–701. https://doi.org/10.1039/b416855k
Marsh, D. R., Janches, D., Feng, W., & Plane, J. M. C. (2013). A global model of meteoric sodium. *Journal of Geophysical Research: Atmospheres*, *118*, 11442–11452. https://doi.org/10.1002/jgrd.50870
Montgomery, J. A., Jr., Frisch, M. J., Ochterski, J. W., & Petersson, G. A. (1999). A complete basis set model chemistry. VI. Use of density functional geometries and frequencies. *The Journal of Chemical Physics*, *110*, 2822–2827. https://doi.org/10.1063/1.477924
Nesvorný, D., Janches, D., Vokrouhlický, D., Pokorný, P., Bottke, W. F., & Jenniskens, P. (2011). Dynamical model for the zodiacal cloud and sporadic meteors. *The Astrophysical Journal*, *743*, 129. https://doi.org/10.1088/0004-637x/743/2/129
Pasek, M. A. (2008). Rethinking early Earth phosphorus geochemistry. *Proceedings of the National Academy of Sciences*, *105*, 853–858. https://doi.org/10.1073/pnas.0708205105
Plane, J. M. C., Feng, W., & Dawkins, E. C. M. (2015). The mesosphere and metals: Chemistry and changes. *Chemical Reviews*, *115*, 4497–4541. https://doi.org/10.1021/cr500501m
Plane, J. M. C., Feng, W., Gómez Martín, J. C., Gerding, M., & Raizada, S. (2018). A new model of meteoric calcium in the mesosphere and lower thermosphere. *Atmospheric Chemistry and Physics*, *18*, 14799–14811. https://doi.org/10.5194/acp-18-14799-2018
Plane, J. M. C., Gomez-Martin, J. C., Feng, W. H., & Janches, D. (2016). Silicon chemistry in the mesosphere and lower thermosphere. *Journal of Geophysical Research: Atmospheres*, *121*, 3718–3728. https://doi.org/10.1002/2015jd024691
Redfield, A. C. (1958). The biological control of chemical factors in the environment. *American Scientist*, *46*, 205–221.
Reinhard, C. T., Planavsky, N. J., Gill, B. C., Ozaki, K., Robbins, L. J., Lyons, T. W., et al. (2017). Evolution of the global phosphorus cycle. *Nature*, *541*, 386–389. https://doi.org/10.1038/nature20772
Saunders, R. W., Dhomse, S., Tian, W. S., Chipperfield, M. P., & Plane, J. M. C. (2012). Interactions of meteoric smoke particles with sulphuric acid in the Earth's stratosphere. *Atmospheric Chemistry and Physics*, *12*, 4387–4398. https://doi.org/10.5194/acp-12-4387-2012
Tobiska, W. K., Woods, T., Eparvier, F., Viereck, R., Floyd, L., Bouwer, D., et al. (2000). The SOLAR2000 empirical solar irradiance model and forecast tool. *Journal of Atmospheric and Solar-Terrestrial Physics*, *62*, 1233–1250. https://doi.org/10.1016/s1364-6826(00)00070-5
Viehl, T. P., Plane, J. M. C., Feng, W., & Höffner, J. (2016). The photolysis of FeOH and its effect on the bottomside of the mesospheric Fe layer. *Geophysical Research Letters*, *43*, 1373–1381. https://doi.org/10.1002/2015gl067241
Vondrak, T., Plane, J. M. C., Broadley, S., & Janches, D. (2008). A chemical model of meteoric ablation. *Atmospheric Chemistry and Physics*, *8*, 7015–7031. https://doi.org/10.5194/acp-8-7015-2008